RESEARCH ARTICLE

A Novel Optimization Framework for High Dynamics Point-to-Point Direct Drive Motion Control System With a New Type of Surrogate Model

CHENTAO TANG[1]**, XIN YIN**[2]**, (Member, IEEE), YOUTONG FANG**[1,3]**, (Senior Member, IEEE), AND PIERRE-DANIEL PFISTER**[1,3]**, (Member, IEEE)**

[1]College of Electrical Engineering, Zhejiang University, Hangzhou 310027, China
[2]Akribis Systems (Hangzhou) Research and Development Center, Hangzhou 310000, China
[3]Zhejiang Provincial Key Laboratory of Electrical Machine Systems, Zhejiang University, Hangzhou 310027, China

Corresponding author: Pierre-Daniel Pfister (pierredaniel.pfister.public@gmail.com)

ABSTRACT A new optimization framework for a high-dynamic point-to-point direct drive motion control system (HDPDMS) is proposed. The conventional system optimization approach considers all design parameters simultaneously, resulting in a high-dimensional search space and extensive computation. In contrast, the proposed framework uses a new DDM surrogate model that establishes a correlation between the key DDM characteristic parameters to decouple the whole optimization process. It begins with a system-level optimization to identify suitable driver types, motion profile design parameters, and characteristic parameters of the direct drive motors (DDMs) by the new surrogate model. Bayesian optimization then determines the DDM design parameters corresponding to the identified characteristic parameters. Once the DDM surrogate model is built, the proposed framework achieved the desired HDPDMS design in just 1 hour, saving 98.6% of computation time compared to the traditional approach. Additionally, multi-objective optimization and Gaussian process regression prediction intervals were employed to obtain a suitable training dataset and input range for the surrogate model, resulting in a 99.8% reduction in computation resources compared to the traditional DDM surrogate model. Through completing three unique motion task optimizations and creating a prototype, the optimization framework was proven effective, demonstrating the potential of this novel method.

INDEX TERMS Point-to-point motion control, direct drive permanent-magnet machine, high dynamics, novel system optimization framework.

I. INTRODUCTION

High-dynamic point-to-point direct drive motion control systems (HDPDMS) have wide industrial applications such as high-speed pick-and-place drives, die bonders, and integrated circuit sorting machines (Fig. 1). An HDPDMS rotates at a specific angle with fast acceleration and deceleration in

The associate editor coordinating the review of this manuscript and approving it for publication was Philip Pong[ID].

milliseconds and then rotates to the next position repeatedly. In the production process, a system may work continuously for more than 20 hours a day with a very high unit per hour (UPH) [1]. Consequently, optimizing the motion control system for higher efficiency is important.

In a typical direct drive motion control system, the load-to-motor inertia ratio is often greater than 20:1. The moment inertia of a direct drive motor (DDM), therefore, does not significantly impact the design requirements for continuous
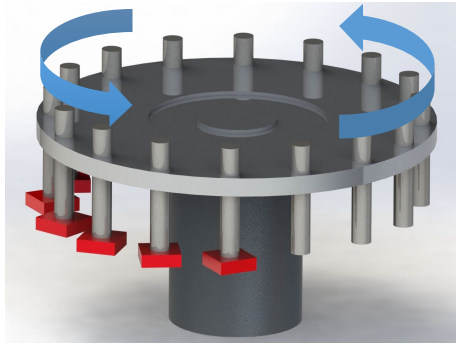
FIGURE 1. High-dynamic point-to-point motion control systems (HDPDMS). Primarily employed in the chip inspection stage, this machine rotates chips at precise intervals for a brief period before pausing for testing, after which it rotates to the next position and repeats the process.
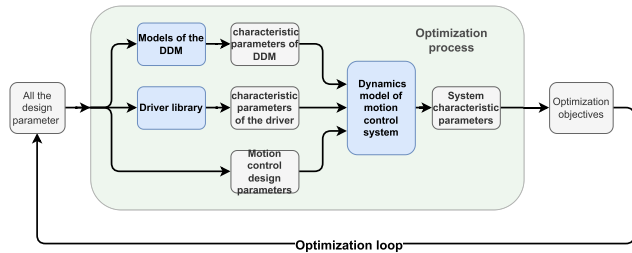

FIGURE 2. Traditional optimization framework of HDPDMS. It includes the DDM, driver, and motion curve three components. All the design parameters and models are used in one big optimization loop.

FIGURE 3. Multi-level optimization framework [2]. The design parameters are separated into two subspaces, and optimizations are done in the motor and control levels successively.

torque, peak torque, and power of the DDM. Additionally, motion times in this system are typically several seconds, allowing the design requirements for the DDM to be directly derived from the motion task and typical motion profiles, such as triangular or trapezoidal waves for acceleration. The proper driver can then be selected based on the required continuous current, peak current, and bus voltage for the DDM design. This approach results in decoupling the design process for the three components.

However, in HDPDMSs, achieving a fast response requires a low load-to-motor inertia ratio, less than 4:1. As a result, the moment inertia of the DDM cannot be ignored. Due to the motion time in the HDPDMS, the motion profile significantly impacts the design requirements for the DDM and driver. The strong coupling between the design requirements of the three components, namely DDM, driver, and motion profile, makes separate designs challenging in HDPDMSs. Therefore, an integrated system optimization approach that considers all three components is necessary for this situation.

The conventional optimization framework for HDPDMSs is shown in Fig. 2. The primary objective of this optimization is to determine suitable design parameters for the DDM, driver, and motion profile for a specific motion task. The optimization of the HDPDMS system poses a significant challenge due to its complex nature, involving a large number of design parameters and constraints for all components. Additionally, the computation burden is increased by the necessity of using finite element methods (FEM) to calculate the DDM's magnetic field. Achieving a
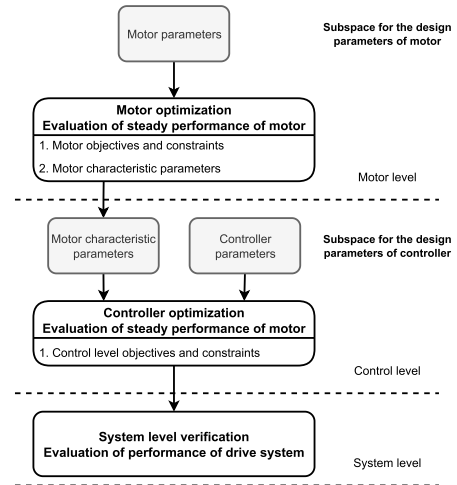
balance between overall cost and system reliability necessitates multi-objective optimization, further compounding the computational demands. Moreover, during the initial design phase, the motion task requires additional adjustments, further contributing to the already substantial computational workload.

Several strategies to reduce computation resources have been proposed, including multi-level optimization frameworks [2], [3], [4], [5], analytical or semi-analytical models [6], [7], [8], [9], [10], and surrogate models [9], [11], [12], [13], [14], [15], [16], [17].

The multi-level optimization framework [2], [3] divides the system into two levels: the motor level and the control level, as shown in Fig. 3. The optimization process involves two levels, starting with optimization for steady-state performances like torque density and efficiency at the motor level, and obtaining characteristic parameters such as resistance, inductance, and flux-linkage for control-level optimization to improve dynamic performances like current rising time and overshoot. This method reduces the computation burden at each level but only works well if the control design parameters do not affect the steady performance parameters of the motor. It is suitable for traction motor systems, for example, in electric vehicles, but proves challenging for HDPDMS as the design parameters of the motion profile and driver influence design requirements of DDM, such as continuous torque, peak torque, and efficiency.

Numerous analytical magnetic field models have been proposed to reduce the computation burden [8], offering the advantage of high generality [6], [18]. For a fixed motor topology, a wide range of design parameters can be changed to obtain different characteristic parameters of the motor. However, these models are limited in their ability to consider the magnetic saturation influence in soft magnetic materials. Analytical or semi-analytical models have a tradeoff between precision and speed to take magnetic

saturation into account [7], [19]. In the case of an HDPDMS, careful consideration of the saturation effect is required for calculating the peak torque, a task that cannot be easily accomplished with fast analytical or semi-analytical models.

The surrogate model is a predictive model trained on information from the sampling points in a training dataset [9], [14], [20]. Once the training is complete, the surrogate model can make accurate predictions quickly and can handle different motion task adjustments to find precise optimization results. However, the 'curse of dimensionality' [12] is challenging for surrogate models. The size of the training dataset increases exponentially with the dimension of the design parameters, making it impractical for the high number of the HDPDMS's design parameters. Therefore, reducing dimensionality is essential for surrogate models. One way is to select critical design parameters based on expert knowledge or perform a sensitivity analysis [21] to identify important design parameters for the surrogate models. However, sensitivity analysis is only effective in a local region with limited ranges for design parameters. Another approach is the sequential optimization method (SOM) [22], [23], which focuses computation resources on the more promising regions with a high probability of containing the optimal solution, similar to Bayesian optimization. However, its effectiveness is limited to a local region, and if the motion task changes, the training dataset needs to be recalculated for the SOM.

In summary, the methods discussed previously have limitations that make them unsuitable for quick and accurate optimization of HDPDMS for different motion tasks with limited computational resources.

After analyzing the traditional optimization framework (Fig. 2), we find that the system-level optimization only requires characteristic parameters of the DDM and driver. The driver's characteristic parameters are fixed once the driver type is selected, leaving the optimization of the DDM's characteristic parameters - such as the phase resistance R_s, phase synchronous inductance L_s, flux-linkage generated by the permanent-magnet (PM) ψ_f, and DDM inertia J_{DDM} to be performed. If we can establish a surrogate model that describes the relationships between these characteristic parameters, such as $\psi_f = S(R_s, L_s, J_{DDM})$, we can perform a system-level optimization to determine the required characteristic parameters of the DDM. Following this, a component-level optimization can be conducted to identify the corresponding design parameters of the DDM that meet the required characteristic parameters. These fundamental ideas of the new optimization framework are illustrated in Fig. 4. Since the dimension of characteristic parameters is typically smaller than that of design parameters, the surrogate model relieves the 'curse of dimensionality' problem and enables quick and accurate system-level optimizations for different motion tasks. As the new surrogate model takes the DDM characteristic parameters as inputs, rather than the design parameters as in traditional surrogate models, the primary challenges of this approach are constructing
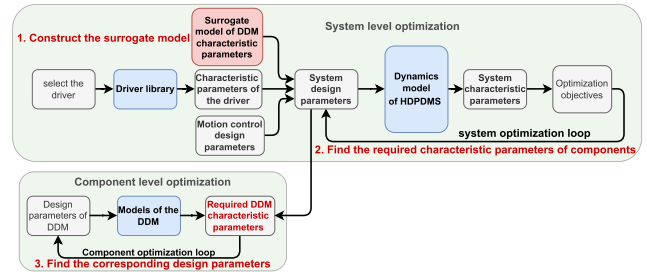

FIGURE 4. The fundamental concepts of the new optimization framework. First, we construct a surrogate model that describes the correlation among the characteristic parameters of DDM. Using this surrogate model, we can perform system-level optimization to determine the required characteristic parameters of DDM. Finally, we conduct a component-level optimization to identify the corresponding design parameters of the DDM that meet the required characteristic parameters.

an appropriate surrogate model for the DDM characteristic parameters, effectively utilizing the surrogate model for system-level optimization, and swiftly retrieving the design parameters of the DDM.

In this article, we define the HDPDMS optimization problem in section II. In section III, we introduce the overview of the new optimization framework. A detailed process of the new optimization is given in section IV. In section V, we provide a comparison between the traditional method and the new method. The prototype and experiment are shown in section VI. Finally, the conclusions are given in section VII.

II. THE DEFINITION OF THE HDPDMS OPTIMIZATION
A. POINT-TO-POINT MOTION TASK AND CONTROL

This article focuses on the point-to-point motion task, which involves rotating a load from position A to position B within a specified time using a DDM. Specifically, we aim to rotate a load with a moment of inertia J_{load} by a specific angle θ_m within a motion time of t_m. After reaching the target position, the machine waits for a dwell time of t_d before moving on to the next position. An S-curve [24] is used to generate the trajectory with two design parameters: the jerk time ratio α_s and the constant speed time ratio β_s, which are shown in Fig. 5. The dynamics model of the S-curve is described by

$$\begin{cases} \dfrac{d\theta_m}{dt} = \omega_m \\ \dfrac{d\omega_m}{dt} = \alpha_m \\ \dfrac{d\alpha_m}{dt} = j_m, \end{cases} \quad (1)$$

where ω_m is the rotational speed, α_m is the rotational acceleration, and j_m is the rotational jerk. In our case, the range of α_s is set from 0.01 to 0.25, and the range of β_s is set from 0.01 to 0.96. They must also satisfy the inequality $4\alpha_s + \beta_s \leq 1$.

The HDPDMS control diagram [25] is shown in Fig. 6. The motion control system comprises three feedback loops: a position loop, a velocity loop, and a current loop. The corresponding loop receives the motion profile generator's
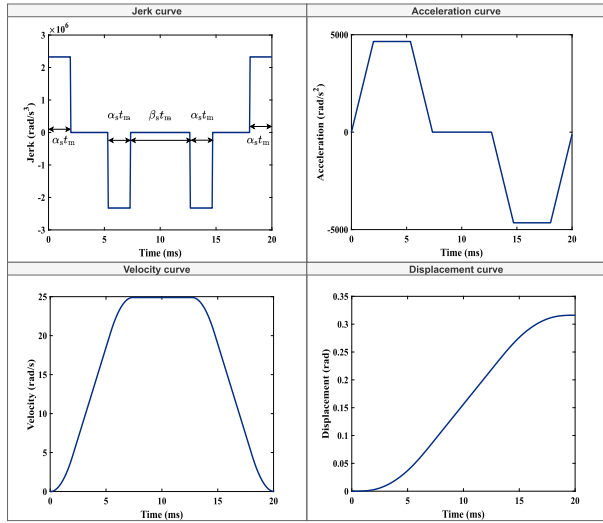
FIGURE 5. The jerk, acceleration, velocity, and displacement curves generated by the S-curve [24]. The variable t_m is the motion time. The expressions $\alpha_s t_m$ and $\beta_s t_m$ are the jerk time and time of constant speed, respectively.

FIGURE 6. The motion control diagram for the HDPDMS. It comprises three feedback loops: a position loop, a velocity loop, and a current loop. The velocity and current feedforward controls are used to increase the dynamic performances of the motion control system.

FIGURE 7. Structure of the surface-mounted PM machine.

FIGURE 8. The mechanical structure of the direct-drive motor includes: the frameless motor, the bearing, the encoder, and the housing.

position, velocity, and acceleration feedforward commands. The position and velocity loops use classical proportional (P) / proportional-integral (PI) controllers, and several low-pass filters are used to reduce high-frequency noise in the velocity loop. The control diagram shown in Fig. 6 uses the $I_d = 0$ control strategy, so the d-axis current is set to zero and ignored. A current controller and space vector pulse width modulation (SVPWM) is employed to drive the motor. Since the motion task is precisely defined and disturbances are minimal, feedforward control dominates this motion control, with feedback control mainly serving to correct unexpected disturbances. In the HDPDMS optimization, we concentrate on the design parameters of the feedforward control, specifically the jerk time ratio α_s and constant speed time ratio β_s in the S-curve motion profile generator.

The dynamics model of the DDM [25] and load is described by the DDM characteristic parameters, like the phase resistance R_s, phase synchronous inductance L_s, flux-linkage generated by the PM ψ_f, and the inertia of the DDM J_{DDR} in

$$\begin{cases} u_d = R_s i_d + L_s \dfrac{di_d}{dt} - P\omega_m L_s i_q \\ u_q = R_s i_q + L_s \dfrac{di_q}{dt} + P\omega_m(L_s i_d + \psi_f) \\ \dfrac{d\omega_m}{dt} = \dfrac{\frac{3}{2}P\psi_f i_q}{J_{load} + J_{DDR}}, \end{cases} \quad (2)$$

where the u_d, u_q, i_d, and i_q are the voltages and currents in the d-axis and q-axis.

B. DDM AND DRIVER
In addition to the motion task and motion control, we must design the DDM and select the proper driver. For the DDM, we use a surface-mounted PM synchronous motor (SPMSM) because it has a high ratio between peak torque and inertia.
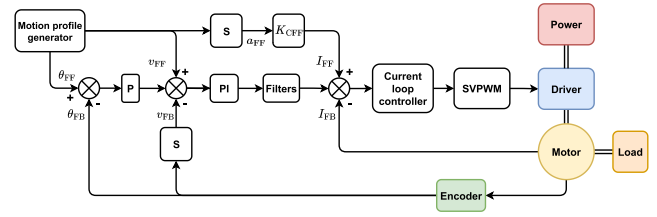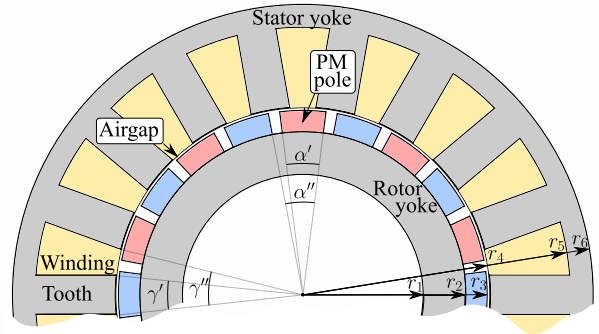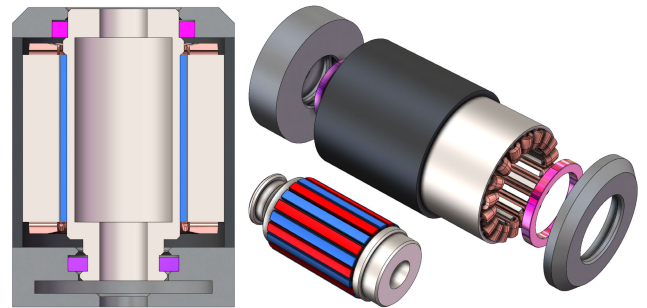
Therefore, it suits well for high dynamics point-to-point motion. Straight teeth are used for easier manufacture and a higher slot-filling factor. The topology and all design parameters of the frameless motor are shown in Fig. 7. The optimization design parameters are listed in Table 1, and the fixed design parameters are shown in Table 2. The design parameters of the housing, bearings, and encoder of the DDM are derived from the design parameters of the frameless motor. The whole structure of the DDM is shown in Fig. 8.

For the magnetic field models of the DDM, except the FEM model, a subdomain model is used to reduce the computation resource of optimization [26]. The subdomain model is a quick and precise semi-analytical model if the magnetic saturation effect is negligible [18]. A thermal network model is used to calculate the temperature of the DDM [27], [28].

We select the driver from a commercial driver library. The library gives the bus voltage V_{bus}, the output continuous current I_{driver}^c, the output peak current I_{driver}^p, and the cost of the driver C_{driver} (Table 3).

TABLE 1. Parameters of the SPMSM machine and their range for optimization. The dimensions are shown in Fig. 7.

Variable	Unit	Min	Max
Current density (J_c)	A/mm^2	7.07	14.14
Thickness of the PMs ($r_3 - r_2$)	mm	3.3	6.6
PM opening angle ratio ($\alpha = \frac{\alpha'}{\alpha''}$)		0.6	1.0
Tooth length ($r_5 - r_4$)	mm	12.4	24.7
Stator yoke thickness, ($r_6 - r_5$)	mm	3.5	7.1
Width of tooth ratio ($\gamma = \frac{\gamma'}{\gamma''}$)		0.4	0.8
Active length (l)	mm	40	160
Outer radius (r_6)	mm	45	90
Inner radius (r_1)	mm	20	60
The total turns of the winding (N_w)		500	2000

TABLE 2. The fixed parameters of the SPMSM machine optimization.

Parameter	Unit	Value
Airgap	mm	0.8
Number of slots		18
Pole pairs		10
PM's remanent magnetic flux density @ 20°C	T	1.43
PM's relative permeability		1.05

TABLE 3. Drivers specifications.

Driver type	Driver A	Driver B	Driver C
Output continuous current (A)	5	10	15
Output peak current (A)	10	20	30
DC bus voltage (V)	310	310	310
Price (RMB)	8k	10k	12k

C. HDPDMS OPTIMIZATION OBJECTIVES AND CONSTRAINTS

A cost indicator and a reliability indicator are taken as the optimization objectives of the HDPDMS optimization. The cost indicator is used to measure the approximate cost of the HDPDMS and operation cost during the operation. It is defined by

$$C = C_{\text{driver}} + C_{\text{DDM}} + C_{\text{operation}}, \qquad (3)$$

where C_{driver} and C_{DDM} are the cost of the driver and motor, respectively. $C_{\text{operation}}$ is the electricity cost of the motion system during the operation time.

Another reliability indicator R is used to measure the reliability of the motion system by the minimum margin for the bus voltage, continuous and peak current of the driver, and the temperature of the winding. We use a negative reliability indicator R. As the optimization involves a minimization,

$$R = -|\min(M_{\text{bus}}, M_c, M_p, M_t)|, \qquad (4)$$

where

- $M_{\text{bus}} = \frac{U_{\text{bus}} - V_{\text{bus}}}{V_{\text{bus}}}$, U_{bus} is the required bus voltage amplitude of the motion system,
- $M_c = \frac{I_{\text{driver}}^c - I_c}{I_{\text{driver}}^c}$, I_c is the required continuous current amplitude of the motion system,
- $M_c = \frac{I_{\text{driver}}^p - I_p}{I_{\text{driver}}^p}$, I_p is the required peak current amplitude of the motion system, and
- $M_t = \frac{T_{\text{max}} - T_{\text{winding}}}{T_{\text{max}}}$, T_{winding} is the average temperature of the winding and T_{max} is the maximum tolerable temperature of the winding. In our case, T_{max} is 100°C.

All of these margins must have negative values to ensure the safe operation of the system, and demagnetization of the PMs must be considered for long-term reliability. These parameters are referred to as the constraints of HDPDMS and are discussed in more detail in the following section. IV-A2.

III. OVERVIEW OF THE NEW OPTIMIZATION FRAMEWORK

A new optimization framework is provided (Fig. 4). The novel optimization framework is based on the DDM characteristic parameters surrogate models. In this section, we address three crucial issues related to this new optimization framework: building the surrogate model of DDM characteristic parameters, utilizing the surrogate model for system-level optimization, and swiftly retrieving the design parameters of the DDM.

A. THE CONSTRUCTION OF THE NEW SURROGATE MODEL

First, we need to select the DDM characteristic parameters in the HDPDMS optimization. For example, the phase resistance R_s, phase synchronous inductance L_s, flux-linkage generated by the PM ψ_f, and the inertia of the DDM J_{DDM} are selected as the DDM characteristic parameters. Second, we need to collect the training dataset for the surrogate models. However, obtaining a training dataset for the surrogate model of DDM characteristic parameters is not as straightforward as it is for the traditional surrogate model, which takes design parameters as inputs. The reason is that the characteristic parameters of the DDM are interdependent, and not all combinations of them exist in reality. For instance, it is impossible to find a DDM with a high value of flux-linkage generated by the PM ψ_f, along with a low value of inertia of DDM J_{DDM}. Therefore, direct sampling of characteristic parameters is not possible.

To address this issue, we set DDM characteristic parameters as optimization objectives in a multi-objective optimization of DDM. The optimization results, located on the Pareto front, comprise the DDM optimization dataset containing physical correlation information. We use this dataset as a training set to build a surrogate model that takes R_s, L_s, and J_{DDM} as inputs and produces ψ_f as a single output. Since the Pareto front exhibits unique properties, the surrogate model $\psi_f = S(R_s, L_s, J_{\text{DDM}})$ is an injective function that can be constructed using Gaussian process regression (GPR) [11] to map the inputs to the output.

The GPR is a non-parametric machine learning algorithm [11]. The advantage of the GPR is that it can not only get the mean value of the prediction but also the variance of the prediction [12].

For a typical regression problem, we have a training dataset (X, y) with m sampling points, where X is an $m \times n$ matrix that includes the m inputs with n-dimensional features, and where $\mathbf{y}$ is an m-dimensional vector which includes the m outputs with a single response. The GPR aims to return the prediction value $\mathbf{f}_*$ corresponding to a new input X_* based on the training dataset. We assume that $\mathbf{y}$ and $\mathbf{f}_*$ satisfy the multi-variables Gaussian distribution in:

$$\begin{bmatrix} \mathbf{y} \\ \mathbf{f}_* \end{bmatrix} \sim \mathcal{N}\left(\mathbf{0}, \begin{bmatrix} K(X, X) + \sigma_n^2 I & K(X, X_*) \\ K(X_*, X) & K(X_*, X_*) \end{bmatrix}\right), \quad (5)$$

where $K(X, X)$ is the covariance function and the variance σ_n^2 of the Gaussian noise is used to model the random noise in the data. In our case, we use the Matern 5/2 covariance function [11]. Every element k_{ij} in $K(X, X)$ is defined in:

$$k_{ij}(x_i, x_j) = \sigma_f^2 \left(1 + \frac{\sqrt{5}r}{\sigma_l} + \frac{5r^2}{3\sigma_l^2}\right)\exp\left(-\frac{\sqrt{5}r}{\sigma_l}\right), \quad (6)$$

where $r = \|x_i - x_j\|$ is the norm between the x_i and x_j, and σ_f and σ_l are hyper-parameters of the GPR.

The mean value and variance of the prediction equations [11] are:

$$\bar{\mathbf{f}}_* \triangleq \mathbb{E}[\mathbf{f}_* \mid X, \mathbf{y}, X_*]$$
$$= K(X_*, X)\left[K(X, X) + \sigma_n^2 I\right]^{-1}\mathbf{y} \quad (7)$$

$$\sigma_m^2 = \text{cov}(\mathbf{f}_*)$$
$$= K(X_*, X_*)$$
$$- K(X_*, X)\left[K(X, X) + \sigma_n^2 I\right]^{-1} K(X, X_*). \quad (8)$$

B. THE UTILIZATION OF THE NEW SURROGATE MODEL IN THE OPTIMIZATION OF THE SYSTEM-LEVEL

Using the mean prediction from (7), we can predict the flux-linkage generated by the PM ψ_f depending on the inputs: the phase resistance R_s, phase synchronous inductance L_s, and the inertia of the DDM J_{DDM}. They can be designated as the optimization variables in the system-level optimization. However, we can not use the arbitrary value of characteristic parameters R_s, L_s, and J_{DDM}. Because the inputs of the surrogate model have an acceptable range. In the case of a traditional surrogate model with design parameters as inputs, determining the acceptable ranges is straightforward, as the design parameters' search space is a box space with minimum and maximum values. However, the input space of the new surrogate model is a projection of the Pareto front onto the characteristic parameters' space. For example, in Fig. 9, a Pareto front of the peak torque T_p, copper loss P_c, and inertia of the DDM J_{DDM} is shown in Fig. 9 (a). This Pareto front is used to build a surrogate model $T_p = S(P_c, J_{DDM})$ to predict the peak torque T_p by the copper loss P_c and inertia of DDM J_{DDM}. The input space of this surrogate
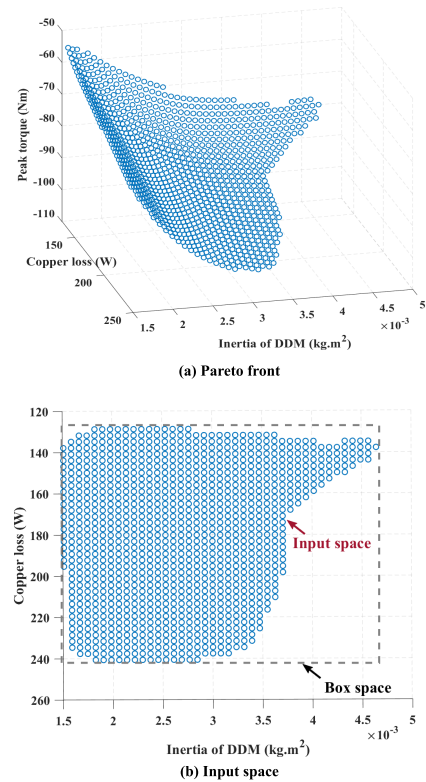

FIGURE 9. Input space of the surrogate model whose inputs are characteristic parameters. The Pareto front between the peak torque, copper loss, and inertia of DDM is shown on the left. The corresponding input space is a projection from the Pareto front to the copper loss and inertia of DDM space.

model is determined by the projection from this Pareto front to the P_c and J_{DDM} space. In Fig. 9 (b), the input space of this surrogate model is irregular. Therefore, we need to find the boundary of input space. The prediction variance of the GPR by (8) is used to find the boundary of the input space.

A 2D function $y = 0.1x^3 + 0.5x^2 + x + \varepsilon$ in Fig. 10 is used as a simple illustration that provides better visualization and an intuitive explanation. This function shape is similar to the Pareto front of the torque and copper loss in the SPMSM. A random noise ε is added to model real data noise. A 95% prediction interval is defined by the $\bar{\mathbf{f}}_* \pm 1.96\sigma_m$. From Fig. 10, we observe that the 95% prediction intervals at the two input boundaries are larger than the middle range of the input. The range of the 95% prediction intervals ΔP is computed in Fig. 11. Statistical analysis is performed on ΔP for the training dataset. Its mean value μ and standard deviation σ are obtained. Threshold 1 and threshold 2 are set as $\mu + \sigma$ and $\mu + 2\sigma$ to determine the input space's boundary. In this research, $\mu + \sigma$ is used as the threshold for better robustness of optimization results.

This method works well when the sampling points on the Pareto front are uniform. If the sampling points on the Pareto is nonuniform, like the situation in Fig. 12, this method fails in some place, as shown in Fig. 13. To avoid this problem,
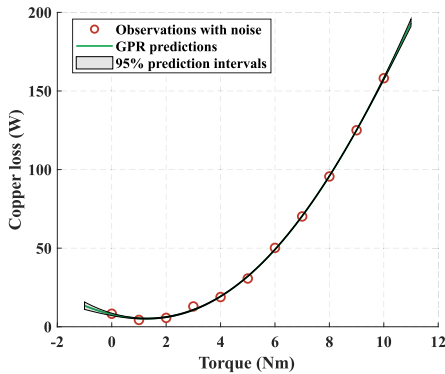
FIGURE 10. 2D Pareto front with uniform sampling. The grey region of 95% prediction intervals at the two input boundaries is larger than in the middle range of the input.
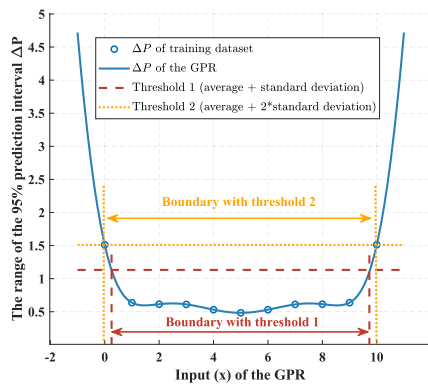

FIGURE 11. The range of the 95% prediction interval (ΔP) with the input for the uniform sampling. Thresholds 1 and 2 are used to determine the boundary of the input of the GPR. All ΔP values are smaller than thresholds 1 and 2 when input is within the boundaries.
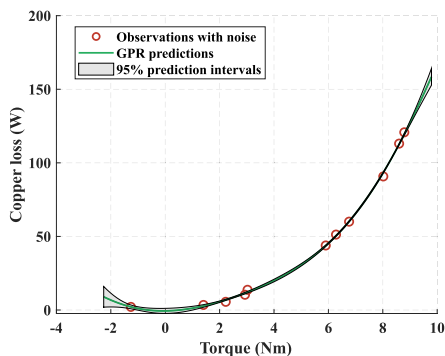

FIGURE 12. 2D Pareto front with nonuniform sampling. The region of 95% prediction intervals is nonuniform, contrary to Fig. 10.

some methods are used in section IV-A to get the uniform Pareto front.

C. RECOVERY OF THE DESIGN PARAMETERS OF DDM
Finally, we need to recover the design parameters of the corresponding DDM with the best characteristic parameters in the system-level optimization. At the system level, we use the DDM characteristic parameters to directly optimize with the new type of surrogate model. The surrogate model only exhibits a correlation between the characteristic parameters of the DDM and does not incorporate any
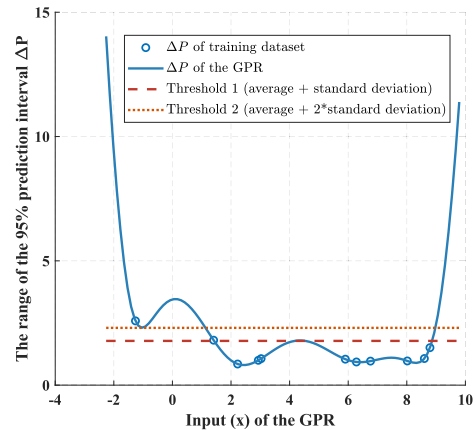

FIGURE 13. The range of the 95% prediction interval (ΔP) for the uniform sampling. Some ΔP values are bigger than threshold 1 or 2, even in places where the input is away from the two sides. Thresholds 1 and 2 cannot determine the boundary of the input of the GPR.
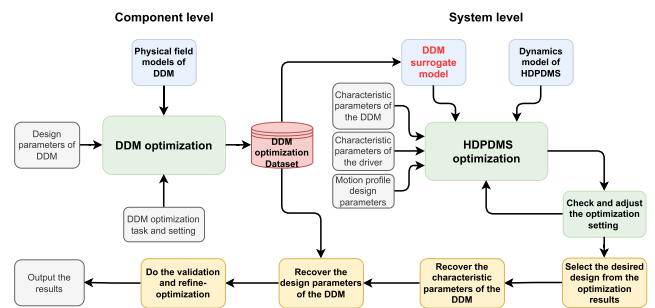

FIGURE 14. The novel optimization framework. It includes four main steps: DDM optimization, constructing DDM surrogate models, HDPDMS optimization, and recovering the design parameters of DDM.

information regarding the corresponding design parameters. Such information is stored in the DDM optimization dataset. With the assistance of the DDM optimization dataset, we use Bayesian optimization [12] to recover the design parameters of the corresponding DDM. The DDM optimization dataset provides the initial samples to build the surrogate model to relieve the cold-start problem of Bayesian optimization. Bayesian optimization makes full use of information from the results during the optimization process to guide the optimization search, which reduces the computation resource.

D. THE NEW OPTIMIZATION FRAMEWORK OF THE HDPDMS
The new optimization framework is shown in Fig. 14 based on the above ideas.

Firstly, we perform multi-objective optimization to obtain the Pareto front of the DDM characteristic parameters. Then, we uniformly sample the optimization results on the Pareto front and store them as the DDM optimization dataset.

Secondly, we build surrogate models of DDM characteristic parameters using the DDM optimization dataset. It is important to note that this surrogate model is used to build the mapping between different characteristic parameters of the DDM and not between the design and characteristic

parameters of the DDM as in traditional surrogate models referenced in [3], [12], and [20].

Thirdly, we perform system-level optimization using the DDM surrogate models and dynamics model of HDPDMS. With the assistance of the DDM surrogate model, this system optimization is quick and precise, and we can easily adjust the driver and motion task to check the optimization results.

Finally, based on the optimization results obtained above, we select a desired design to recover the design parameters of the DDM. Using the DDM optimization dataset and Bayesian optimization, we can quickly recover the design parameters of the DDM and perform the final validation check of the entire system design.

The next section will provide a detailed and specific method for performing the above optimization process.

IV. OPTIMIZATION PROCESS OF THE NEW FRAMEWORK

A. COMPONENT-LEVEL OPTIMIZATION AND SURROGATE MODEL OF THE DDM

1) SELECTION OF THE CHARACTERISTIC PARAMETERS OF THE DDM

First, we select the characteristic parameters of the DDM as the optimization objectives. In (2), four characteristic parameters, phase resistance R_s, phase synchronous inductance L_s, flux-linkage generated by the PM ψ_f, and the inertia of the DDM J_{DDM}, are used to describe the dynamics model of the DDM. The flux-linkage generated by the PM ψ_f should be a function of the current in the q-axis for the SPMSM to consider the magnetic saturation. Hence, the peak torque T_p, peak current I_{motor}^p, continuous torque T_c, and continuous current I_{motor}^c are selected as the characteristic parameters to replace the ψ_f. In this article, we set the peak current I_{motor}^p to three times the continuous current I_{motor}^c. The corresponding torques are peak torque T_p and continuous torque T_c. The cost of the DDM C_{DDM} and copper loss P_c are also needed to compute the cost and reliability indicators in the system-level optimization. Therefore they are added to the list of characteristic parameters.

These nine characteristic parameters have some redundant information. The continuous current $I_{motor}^c = \sqrt{\frac{P_c}{3R_s}}$ is related to P_c and R_s. The peak current I_{motor}^p is three times higher than I_{motor}^c. To reduce the computational burden of multi-objective optimization, we have selected the most important characteristic parameter among the rest of the seven parameters. Since point-to-point motion control systems are primarily limited by their peak torque and not their continuous torque, we have chosen peak torque T_p as the key characteristic parameter.

In an SPMSM, the electromagnetic dynamics are determined by the synchronous phase inductance L_s and the phase resistance R_s of the motor's stator windings. The synchronous phase inductance L_s plays a more crucial role than the phase resistance R_s in determining the response speed of the electromagnetic dynamics in an SPMSM. The minimum jerk time $t_{min}^{jerk} = \alpha_{min} T_m$ is used to evaluate the minimum time

from the start to the maximum torque T_{max} in the motion control. A smaller minimum jerk time t_{min}^{jerk} corresponds to a quicker dynamic response ability of the motor. For the SPMSM, the $I_d = 0$ current control strategy is used. The speed of the motor is relatively low from the start to the t_{min}^{jerk} and the EMF can be neglected during the current rising time. Based on the above analysis, the q-axis voltage in (2) can be simplified into $u_q \approx R_s i_q + L_s \frac{di_q}{dt}$. The q-axis current is given by $i_q(t) = \frac{U_q}{R_s}(1 - e^{-\frac{R_s}{L_s}t})$, where U_q is the drivers's maximum voltage on the q-axis. Based on this equation, the minimum jerk time t_{min}^{jerk} can be derived from

$$t_{jerk}^{min} = \ln\left((1 - \frac{T_{max}R_s}{K_t U_q})^{-\frac{L_s}{R_s}}\right), \tag{9}$$

when the maximum torque T_{max} in the motion control is reached, where the K_t is the motor's torque constant.

The maximum torque T_{max} should be less than the peak torque T_p, and the voltage drop on the resistance should be less than the maximum voltage on the q-axis U_q, if the proper driver is used. Therefore, $\frac{T_{max}R_s}{K_t U_q} < \frac{T_p R_s}{K_t U_q} = \frac{I_p R_s}{U_q} < 1$. We use the Taylor series for the function $f(x) = (1+x)^\lambda$ centered at $x = 0$, where $\lambda \in \mathbb{C}$ and $|x| < 1$:

$$(1+x)^\lambda = \sum_{k=0}^{\infty} \binom{\lambda}{k} x^k$$
$$\binom{\lambda}{k} = \frac{\lambda(\lambda-1)(\lambda-2)\cdots(\lambda-k+1)}{k!}, \tag{10}$$

to approximate the minimum jerk time by (11). By selecting the first two series, we obtain

$$t_{jerk}^{min} = \ln\left(1 + \frac{T_{max}L_s}{K_t U_q}\right). \tag{11}$$

Based on this equation, the t_{jerk}^{min} does not depend on the phase resistance R_s. Therefore, the synchronous phase inductance L_s is the more important characteristic parameter that reflects the response speed of the electromagnetic dynamics in an SPMSM.

In conclusion, the five important characteristic parameters T_p, L_s, J_{DDM}, P_c and C_{DDM} are selected.

2) MULTI-OBJECTIVES OPTIMIZATION OF DDM

Based on the above analysis, characteristic parameters T_p, L_s, J_{DDM}, P_c, and C_{DDM} are selected as the optimization objectives. The resistance and PMs are subject to temperature effects, with peak torque T_p and copper loss P_c in particular being sensitive to temperature. During DDM optimization, we aim to maintain the winding temperature at around 75℃. As the torque, the loss, and the resistance are all dependent on temperature, it is essential to maintain a consistent temperature for the DDM optimization dataset. Based on the dataset, this allows for the calculation of designs with varying temperatures during system-level optimization, assuming that the motor's equivalent thermal resistance remains constant when the winding temperature is between 50℃ and 100℃.
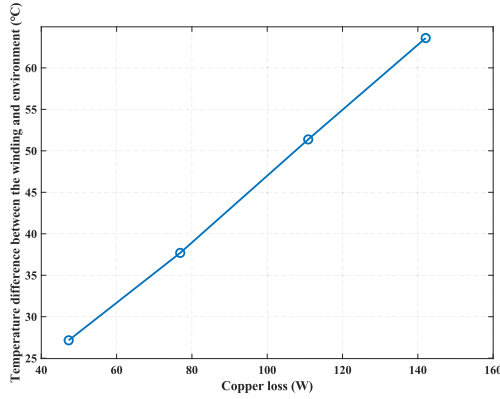
FIGURE 15. The temperature difference between the winding and the environment and the copper loss obtained from the experiment. The gradient of this curve represents the equivalent thermal resistance of the motor, which remains constant in the range of 50°C to 100°C for the winding temperature. The experiment was conducted at an ambient temperature of 28.3°C.

To verify this assumption, we made an experiment to measure the equivalent thermal resistance. Figure 15 shows the relationship between copper loss and the temperature difference between the winding and the environment. For this experiment, the ambient temperature of the experiment was 28.3°C. The slope of the curve is the equivalent thermal resistance of this motor. It is close to a constant at different temperatures.

Based on the above analysis, the constraint for the winding temperature range has been established. The lower and upper constraints of the winding temperature are set at 70°C and 80°C, respectively. The constant equivalent thermal resistance assumption is used to correct the T_p and P_c to keep the winding temperature equal to 75°C. The k_{PM} is used to do the thermal correction for the PMs in

$$k_{PM} = 1 - \alpha_{PM} \left(\frac{75°C - T_a}{T_w - T_a}(T_{PM} - T_a) + T_a - 20°C \right),$$
(12)

where T_w, T_{PM}, and T_a are the temperature of the winding, PMs, and environment, respectively. The variable α_{PM} is the thermal coefficient of the remanence in the PM which is equal to 0.11% in our case.

The variable $k_{current}$ is used to do the thermal correction for the current by

$$k_{current} = \frac{I_{75°C}}{I_{T_w}} = \sqrt{\frac{(75°C - T_a)R_{T_w}}{(T_w - T_a)R_{75°C}}},$$
(13)

where $I_{75°C}$ and I_{T_w} are the current when winding temperatures are equal to 75°C and T_w, respectively. The phase resistances R_{T_w} and $R_{75°C}$ are obtained from $R_T = (1 + \alpha(T - T_a))R_{T_a}$ at the different winding temperatures, where $\alpha = 0.00385$ is the temperature coefficient of copper resistivity when the ambient temperature T_a is 25°C. Equation (13) is derived from $\frac{I_{75°C}^2 R_{75°C}}{I_{T_w}^2 R_{T_w}} = \frac{75°C - T_a}{T_w - T_a}$, based on the constant equivalent thermal resistance assumption.

In our case, we assume that the peak torque T_p is proportional to the current and remanence of the PM when the current and temperature is changed in a small range. Through this assumption, the peak torque T_p is correct by the k_{PM} and $k_{current}$:

$$T_p = k_{PM}k_{current}T_p^o,$$
(14)

where T_p^o is the original value of the peak torque when the motor is at ambient temperature.

In the same way, the copper loss P_c can be derived from

$$P_c = k_{current}^2 \frac{R_{75°C}}{R_{T_w}}P_c^o = \frac{(75°C - T_a)}{(T_w - T_a)}P_c^o,$$
(15)

where P_c^o is the original value of the copper loss when the temperature of the motor is at ambient temperature.

The demagnetization is set as a constraint to ensure the reliability of the DDM. A current four times the value of the continuous current is used to check the demagnetization of the PM. For the cost consideration, the PM volume ratio upper $\alpha_{PM} = \frac{V_{PM}^{max}}{V_{Motor}}$ is set as the constraint, where V_{PM}^{max} is the maximum volume of the PM and V_{Motor} is the volume of the motor. In our case, the α_{PM} is equal to 0.074.

The cost of the motor encompasses a variety of factors, such as material costs, labor expenses, manufacturing expenses, and auxiliary fixtures. To simplify the computation, we assume that the cost of the motor is directly proportional to its volume, considering the PM volume ratio constraints. In this study, we adopt a price of 920 RMB per liter as the unit price for the motor volume. Note that this cost function can vary based on the manufacturing company and the market, but it does not affect the primary conclusions of this article.

The phase resistance R_s and synchronous phase inductance L_s are related to the total turns of winding N_w. In the same motor, the relationships of the phase resistance and synchronous phase inductance with different winding turns are

$$R_s = \left(\frac{N_w}{N_o} \right)^2 R_{so},$$
(16)

and

$$L_s = \left(\frac{N_w}{N_o} \right)^2 L_{so},$$
(17)

where R_{so} and L_{so} are the original resistance and inductance with the original total turns of winding N_o.

In the DDM optimization, we fix the total turns of winding N_w as N_o and compute the phase resistance and inductance as R_{so} and L_{so}. Then, we can use (16) and (17) to compute phase resistance R_s and synchronous phase inductance L_s, when we change the total turns of winding N_w in the system-level optimization. Therefore, N_w is removed from the design parameters in the DDM optimization. The remaining 9 design parameters in Table 1 are used for DDM optimization.

The bi-criterion evolutionary optimization algorithm (BCE-IBEA) [29] is used. It combines the indicator-based and non-dominated optimization algorithm advantages to
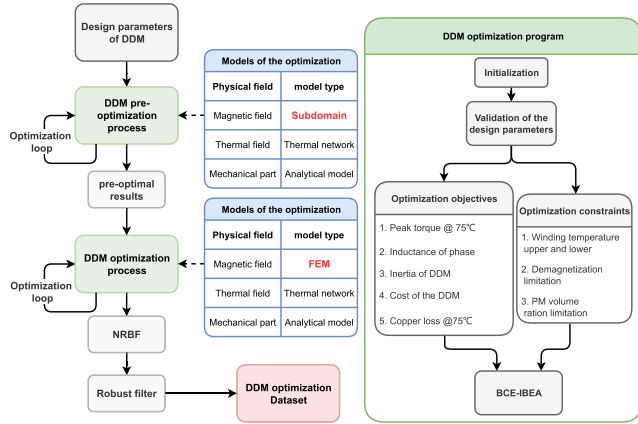
FIGURE 16. DDM optimization framework. The pre-optimization with the quick subdomain is performed first. The next optimization with FEM inherits the pre-optimal results as the initial design. The BCE-IBEA [29], NRBF, and robust filters [26] are used to get uniform sampling on the 5D Pareto front to generate the DDM optimization dataset.

give a better diversity of the results in the Pareto front. A pre-optimization uses a subdomain model for the magnetic field computation to get the pre-optimal results. They are further optimized using the FEM for magnetic field computation. This method reduces the computation resource by about 70% [26]. The population is 210, and the number of generations is 400 and 100 for the optimization using the subdomain model and FEM, respectively. Most of the time is spent on the 100 generations optimization with the FEM model. Its computation resource is $210 \times 100 = 21\,000$ cases. A single computation case involves computing the magnetic and thermal models for a single DDM design. The niche-radius-based filter (NSBF) and robust filter [26] are used to get uniform sampling on the Pareto front based on the optimization results from the different generations. Finally, the DDM optimization dataset is obtained. It includes the design parameters and the corresponding optimization objectives T_p, L_s, J_D, P_c, and C_{DDR}, such characteristic parameters. The framework of the DDM optimization is shown in Fig. 16.

3) SURROGATE MODELS OF CHARACTERISTIC PARAMETERS OF THE DDM

After the muti-objectives optimization of the DDM, the surrogate models of the characteristic parameters are built based on the uniform sampling on the Pareto front. The theory of GPR and simple 2D Pareto front examples were shown in sections III-A and III-B. We expand these ideas for the important DDM characteristic parameters to get the 5D Pareto front and corresponding surrogate models. The framework of the surrogate models of DDM characteristic parameters is shown in Fig. 17.

The peak torque T_p is selected as the output of the surrogate model, and the remaining four characteristic parameters are set as the inputs of the surrogate model in

$$T_p = \mathrm{GPR}_{T_p}(L_s, J_D, P_c, C_{DDR}). \qquad (18)$$
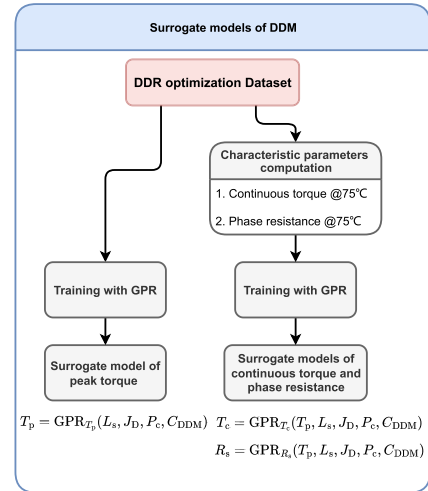

FIGURE 17. The construction of the surrogate models for the characteristic parameters. The three surrogate models are built to predict the peak torque T_p, the continuous torque T_c, and the phase resistance R_s.

The phase resistance R_s and continuous torque T_c surrogate models are also built for system-level optimization. Firstly, we compute the corresponding variables R_s and T_c for the optimal designs uniformly spread on the Pareto front. We apply thermal corrections to these variables, just as we do for P_c and T_p. Finally, we use the five important characteristic parameters as inputs and set R_s and T_c as outputs to build surrogate models using GPR:

$$T_c = \mathrm{GPR}_{T_c}(T_p, L_s, J_D, P_c, C_{DDR}) \qquad (19)$$

$$R_s = \mathrm{GPR}_{R_s}(T_p, L_s, J_D, P_c, C_{DDR}). \qquad (20)$$

The prediction error distributions of the surrogate models for the variables T_p, R_s, and T_c are shown in Fig. 18. The precision of the the T_p and T_c surrogate models is high. The average errors are about 0.8% and 0.4%, respectively. The precision of the R_s surrogate model is lower. Its average error of it is about 3.5%. Nevertheless, it does not play a critical role in system-level optimization.

B. SYSTEM-LEVEL OPTIMIZATION FOR HDPDMS

After the completion of surrogate models for the DDM characteristic parameters, the optimization of HDPDMS at the system level is performed. The framework of the system-level optimization for the HDPDMS is shown in Fig. 19.

1) HDPDMS OPTIMIZATION PROCESS

The optimization variables of the HDPDMS include synchronous phase inductance L_s, the inertia of DDM J_D, copper loss P_c for a winding at 75℃, the volume of the DDM C_{DDR}, the jerk time ratio α, the constant speed time ratio β, and the winding turns of the DDM N_w. Using the surrogate models of DDM characteristic parameters, the peak torque T_p, continuous torque T_c, and phase resistance R_s are computed in less than 1 ms.
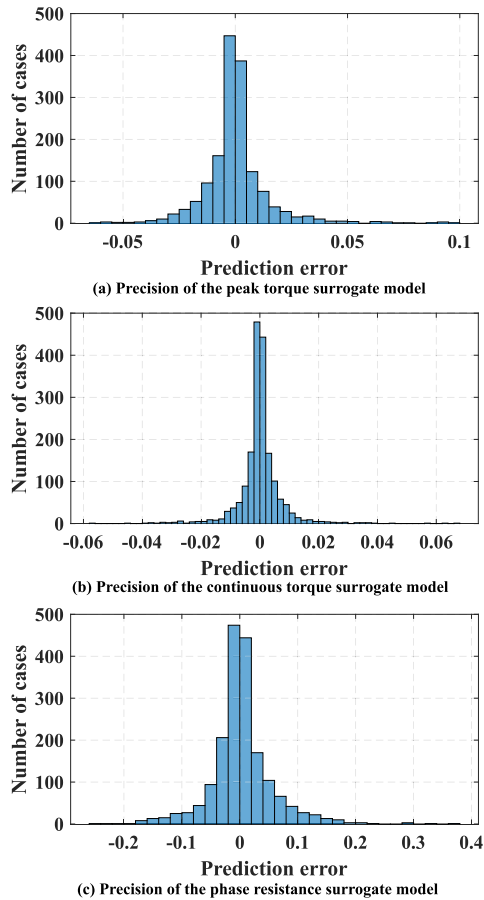
FIGURE 18. Precision of the surrogate models of the peak torque T_p, continuous torque T_c and phase resistance R_s. The precision of the T_p and T_c surrogate models is high. The average errors are about 0.8% and 0.4%, respectively. The precision of the R_s surrogate model is lower. Its average error of it is about 3.5%. Nevertheless, it does not play an important role in system-level optimization.
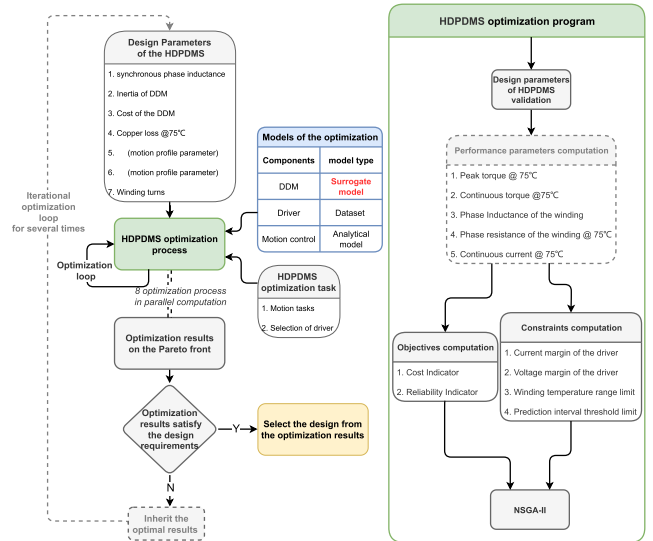

FIGURE 19. The optimization variables in the HDPDMS optimization include the DDM characteristic parameters, motion curve design parameters, and winding turns. Eight independent optimization processes are computed in parallel to decrease the effect of the randomness of the evolutionary optimization algorithm NSGA-II. If the optimization results do not satisfy the design requirements, the next optimization inherits the optimal results and performs further optimization searches.

To begin, we use the dynamics model of HDPDMS to calculate both the current and voltage curves. We derive the continuous current from the current curve to determine the loss. Next, by assuming a constant thermal resistance, we determine the winding temperature and refine the loss through multiple iterations. Ultimately, the HDPDMS is optimized by considering both its cost indicator and reliability indicator defined in (3) and (4). The price of the different drivers is shown in Table 3. The electricity cost of the motion system $C_{operation}$ is based on the following assumption. The motion system operates 20 hours a day and works for three years with 1 RMB / kWh.

The current and voltage margins of the driver are set as constraints to keep the feasibility of the motion system. The maximum winding temperature is set to 100°C to keep the safety of the DDM. A winding lower temperature of 50°C is also set as the constraint to reduce the search space. This also ensures that the assumption that equivalent thermal resistance is constant when winding is from 50°C to 100°C can be used. The 95% prediction interval of the T_p surrogate model should be less than the threshold defined in section III-B.

We established it as a constraint to ensure the existence of the DDM with these characteristic parameters in reality.

The NSGA-II [30] is selected as the optimization algorithm. The population of every generation is 30, and the number of generations is 150. Eight independent optimization processes are computed parallelly to decrease the effect of the randomness of the evolutionary optimization algorithm. Then, all the datasets from the optimization processes are combined and sampled uniformly on the Pareto front. Finally, the motion designer can check the optimization results. If the results are unsatisfactory, the next optimization process can use these optimal results as the initial design to do a further optimization search until the optimization results satisfy the requirement.

2) HDPDMS OPTIMIZATION PARETO FRONTS
With the assistance of the surrogate models for the characteristic parameters of the DDM, the system-level optimization of the HDPDMS can be done quickly. Approximately five iterations of the optimization process above are required to obtain the convergence Pareto front for a particular motion task and driver within 15 minutes. All computation was made on an AMD 3700X with eight cores which runs at 4.2 GHz. Three different motion tasks and three different drivers are selected to do the optimization. The three motion tasks and three drivers are shown in Tables 3 and 4. Motion task 1 is typical for the HDPDMS commonly used in industry. Motion task 2 is a relatively quick motion with a light load and long dwell time. Motion task 3 is a relatively low motion with a heavy load and short dwell time.

The Pareto fronts of the different motion tasks with the different drivers are shown in Figs 20, 22, and 21.

TABLE 4. Motion tasks.

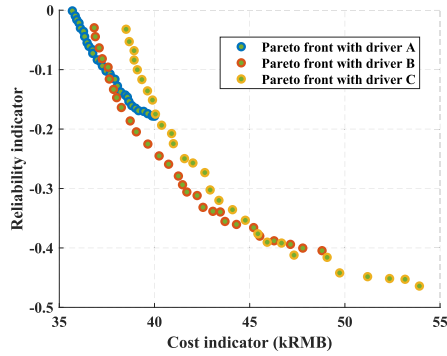| Motion task 3	Task 1	Task 2	Task 3
Displacement (°)	18	18	60
Motion time (ms)	20	15	150
Dwell time (ms)	40	45	30
Inertia of load (kg.m²)	0.01	0.0035	0.25

FIGURE 20. The optimization results for motion task 1 are presented for three drivers, where the driver with a higher volume is associated with a greater reliability margin and cost. Driver A provides the lowest cost indicator for reliability margins of less than 10%. Driver B offers the best design solutions for reliability margins between 10% and 38%. However, if the reliability margin needs to be greater than 40%, driver C is the preferred option.
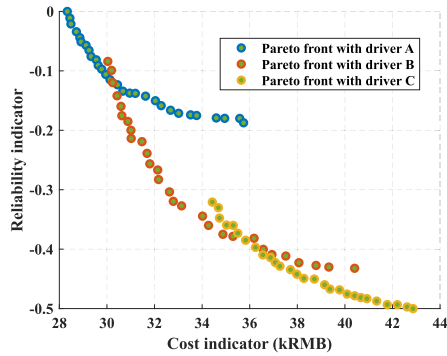

FIGURE 21. The optimization results for motion task 2 using three different drivers show that the volume of drivers significantly impacts the performance of relatively quick motions. Notably, the Pareto front varies across the different driver types. Driver A is the recommended option for instances where the reliability margin is less than 12%. In cases where the reliability margin falls between 12% to 35%, driver B yields the best candidate designs. However, driver C should be selected for situations where a reliability margin of more than 40% is required.

Based on the results of the above experiments, we find that the proposed new system optimization gets good Pareto fronts for different motion tasks and drivers. Every motion task needed approximately 15 minutes to get the optimization Pareto front. The motion system designers can select the desired HDPDMS design from the Pareto front based on their expert experience.

C. DESIGN PARAMETERS RECOVERY

In the system-level optimization, a desired HDPDMS design is selected in the Pareto front. The design parameters of the DDM are needed to recover for this HDPDMS design. In this
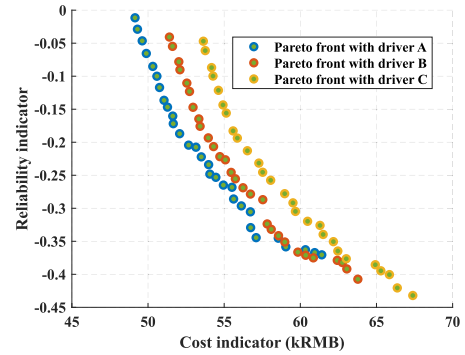

FIGURE 22. The motion task 3 optimization results for three different drivers demonstrate that the relatively low motion is not sensitive to the volume of drivers. All the drivers can provide suitable designs when the reliability margin is within the range of 5% to 40%. However, driver A is preferred for achieving the smallest cost indicator designs.

step, we recover the design parameters of the DDM with the assistance of the DDM optimization datasets and Bayesian optimization. The framework of the recovery process is shown in Figs 23 and 24.

1) RECOVERY OF THE DESIGN PARAMETERS WITH THE ASSISTANCE OF THE DDM OPTIMIZATION DATASET

The selected DDM is called the expected design. The DDM characteristic parameters in the expected design can be set as a vector $V_{\text{expected}} = [T_{\text{p}}, L_{\text{s}}, J_{\text{DDM}}, P_{\text{c}}, C_{\text{DDR}}]$. The characteristic parameters of every DDM in the DDM optimization dataset can be set as a vector V_{DDM}^{n}, where n is the serial number of DDM in the dataset.

The distance $d = |\frac{V_{\text{expected}} - V_{\text{DDM}}^{n}}{V_{\text{expected}}}|$ can be computed. Then, the DDM with the minimum d can be found, called the recovered design. This recovery method is called the 'closest point'. Finally, the whole motion system can be validated with the recovered design parameters to get the corresponding cost $C_{\text{recovered}}$ and reliability indicator $R_{\text{recovered}}$. In this step, we do not use the constant equivalent thermal resistance assumption. The validation is performed based on the design parameters of the recovered design by the iterative computation with magnetic, thermal, and motion control dynamics models. The difference in the temperature of the winding between this computation and the last computation is given by $\Delta T = |\frac{T_{\text{w}} - T_{\text{w}}^{\text{o}}}{T_{\text{w}}^{\text{o}}}|$, where T_{w} is the temperature of the winding and T_{w}^{o} is the temperature of the winding in the last computation. Finally, the optimization objectives of the recovery design are output until the ΔT is less than 0.1%.

The optimization objectives of the expected design and recovery design are set as a vector $O_{\text{expected}} = [C_{\text{expected}}, R_{\text{expected}}]$ and $O_{\text{recovered}} = [C_{\text{recovered}}, R_{\text{recovered}}]$. If the distance $\Delta D = |\frac{O_{\text{expected}} - O_{\text{recovered}}}{O_{\text{expected}}}|$ is less than 0.02, we output this recovered design. Otherwise, we use Bayesian optimization to do the refined optimization.

2) REFINE-OPTIMIZATION WITH BAYESIAN OPTIMIZATION

Based on the recovered design from the above process, we can do the refined optimization to reduce the distance ΔD.
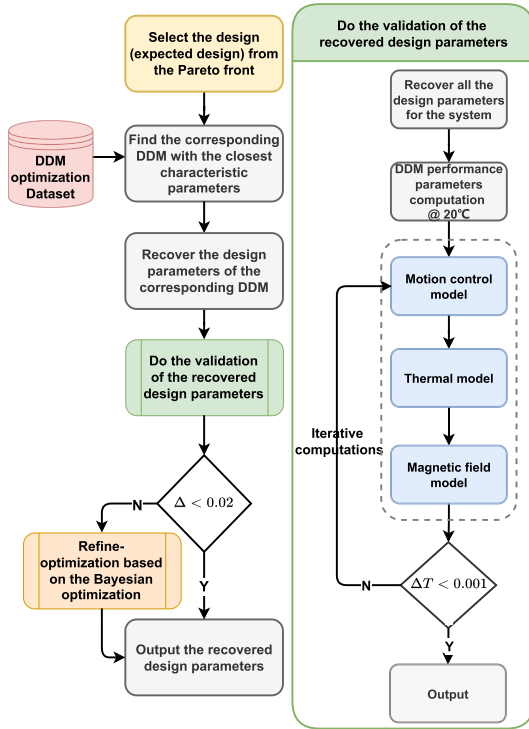
FIGURE 23. Design parameters recovery framework. To recover the design parameters, we use the DDM optimization dataset to identify the DDM with the characteristic parameters closest to the target design. The validity of the recovered design parameters is assessed through iterative computations involving magnetic, thermal, and motion control dynamics models. If the distance between the recovered and target design parameters, denoted as ΔD, is less than 2%, the recovered design parameters are considered acceptable and output. However, if ΔD exceeds 2%, we use Bayesian optimization to refine the recovered design parameters.
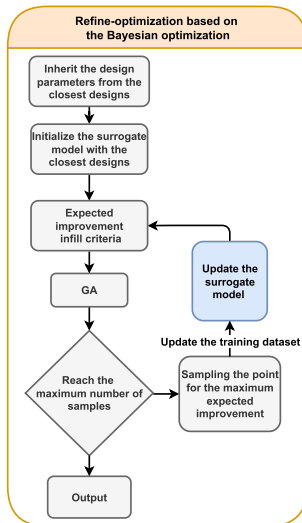

FIGURE 24. To train the local surrogate model of the distance ΔD, we use the closest designs with the expected designs from the DDM optimization as the training dataset. The expected improvement infill criteria [12] is employed in combination with the genetic algorithm (GA) [31] to determine new samples and update the surrogate model iteratively until the maximum number of samples is reached.

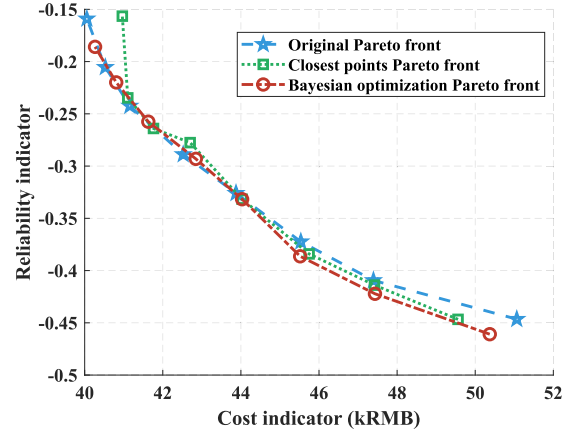The Bayesian optimization is selected to do the refine optimization.

FIGURE 25. Comparison between the original and recovered Pareto fronts. In the figure, the expected designs are denoted by star points, while the designs found using the closest points method with the DDM optimization dataset are marked by square points. The round points represent the designs obtained through Bayesian optimization. All of these recovered designs are close to the expected designs, but those obtained from Bayesian optimization are the closest.

First, we get the closest 30 designs by sorting the distance d in the DDM optimization dataset. The distance ΔD of these 30 designs is computed. The GPR is selected to build the surrogate model between the design parameters of DDM and distance ΔD. The expected improvement infill criteria [12] are used to determine the next sampling. The genetic algorithm (GA) [31] is selected, and 100 generations with eight populations are used to optimize to get the maximum expected improvement. Then, the new sampling is added to the training dataset, and update the surrogate model of distance ΔD until the number of the new sampling reaches 30. We recovered the design parameters of DDM within about 15 minutes.

3) RECOVERED DESIGNS RESULTS

As an example, the Pareto front of motion task 1 and driver C are selected to recover the design parameters. We sampled eight points on the original Pareto front and recovered their design parameters. The result is shown in Fig. 25. From the figure, we can find that the Pareto front with the closest point method is close to the original Pareto front. All of the Pareto front with Bayesian optimization are better than the Pareto front with the closest point method and are closer to the original Pareto front.

V. COMPARISON WITH TRADITIONAL METHODS
A. COMPARISON WITH THE TRADITIONAL OPTIMIZATION FRAMEWORK

A comparison result between the new and traditional optimization framework is performed. The traditional HDPDMS optimization framework is shown in Fig. 26.

The traditional optimization framework used the same range of design parameters as those of the new framework, as seen in Table 1. The optimization objectives and constraints were also the same as those outlined in section IV.
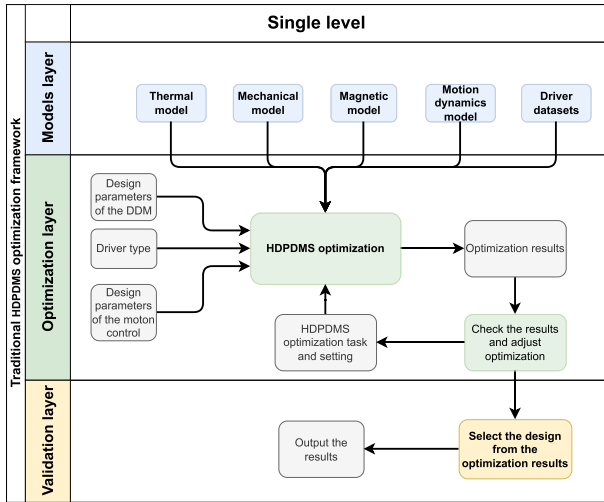
FIGURE 26. The traditional HDPDMS optimization framework. There is only one level in the traditional framework. All the design parameters and models are combined into one optimization. The optimization layer bears the entire burden of computation.
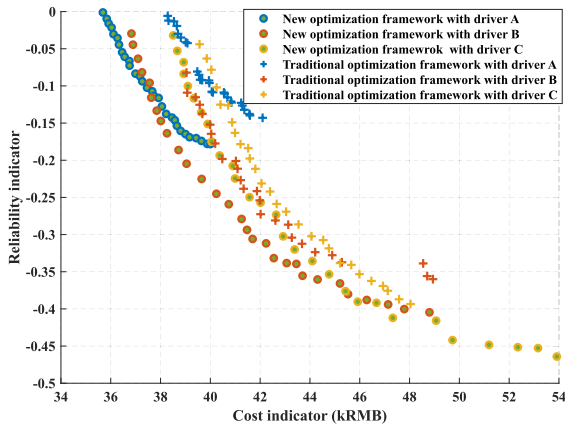

FIGURE 27. Comparison of optimization results between the new and traditional frameworks. The new optimization framework demonstrates better convergence and a wider coverage range compared to the traditional framework, despite utilizing similar computational resources.

Motion task A was selected, and three optimizations were performed using different drivers. For a fair comparison, the traditional optimization framework used the same computation resource of 240 generations and 30 populations with the optimization algorithm NSGA-II. This computation resource was equivalent to 21 600 cases (calculated as $240 \times 30 \times 3$), comparable to the 21 000 cases needed by the new optimization framework to obtain the DDM optimization dataset. The optimization results of the new and traditional optimization frameworks are depicted in Fig. 27. The new optimization framework showed better convergence and a wider coverage range compared to the traditional framework.

The new optimization framework needs 72 hours to collect the DDM optimization dataset. After completing the optimization dataset, the new optimization framework generates the Pareto front for one driver type in just 15 minutes and takes an additional 15 minutes to recover the design parameters of the desired DDM. For a single optimization

task, which involves optimizing three types of drivers and recovering design parameters, the total time is included. The HDPDMS optimization is completed within 1 hour using the new framework. In contrast, the traditional optimization framework takes approximately 72 hours to accomplish the same optimization task. For a single optimization task, the new optimization framework can save about 98.6% computation time. The benefits of the new optimization framework become increasingly apparent as the number of motion tasks increases. This will be a powerful tool for the initial design phase requiring numerous adjustments to the motion control system.

Compared to the traditional optimization framework, which combines all the design parameters, models, and constraints to do the optimization, the comprehensive new optimization framework shown in Fig. 28 allows for a separate optimization process at the component level and system level. This is made possible by the new surrogate model of characteristic parameters that decouples the component-level and system-level optimizations. In the component-level optimization, the focus is solely on optimizing DDM to achieve better characteristic parameters without considering the influence of the driver and motion profile. In system-level optimization, the surrogate models provide a physical correlation of the DDM characteristic parameters, enabling the use of characteristic parameters for HDPDMS optimization directly. Compared to the traditional framework, the new framework uses fewer design parameters, models, and constraints in each optimization level, reducing the optimization burden and producing better optimization results, as shown in Fig. 27.

B. COMPARISON WITH THE TRADITIONAL SURROGATE MODEL

If the traditional surrogate model is used for the DDM, the inputs are the design parameters of DDM, and the outputs are characteristic parameters which include T_p, T_c, L_s, and demagnetization. The four surrogate models need to be built, respectively. The dimension of the design parameters of DDM is nine. If the full factorial sampling with the six samples on every dimension is performed, the total size of the training dataset is $6^9 = 10\,077\,696$ cases. The required number of samples significantly exceeds the computational resource of a new surrogate model, which is only about 21 000 cases. The new optimization framework saves 99.8% of computation resources. The SPMSM represents the simplest topology among PM motors. More complex topologies of PM motors require additional design parameters, exacerbating the computational resource issue.

The new surrogate model is a new form of dimension reduction strategy. However, unlike traditional methods outlined in Section I, which directly reduce the number of design parameters, the new surrogate model achieves dimension reduction by transforming the search space from the design parameters space to the characteristic parameters
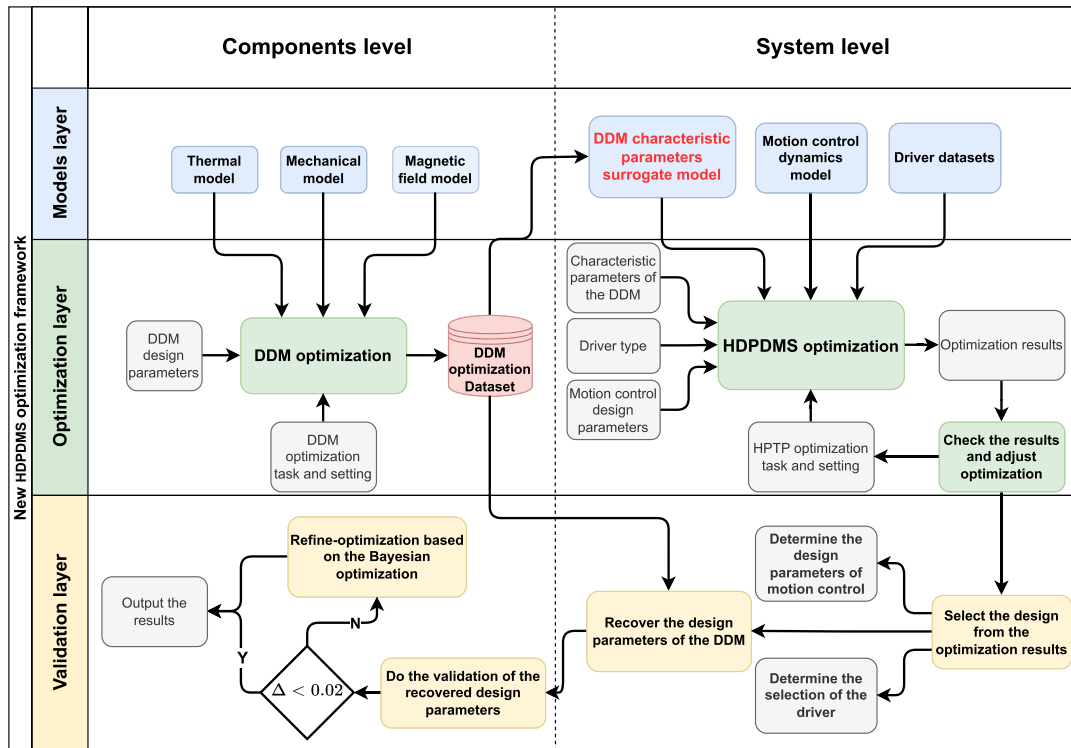
FIGURE 28. The complete new HDPDMS optimization framework. The new framework allows for more efficient optimization at both component and system levels, thanks to a decoupled surrogate model of DDM characteristic parameters. This model enables independent optimization of the DDM at the component level, without considering the influence of the driver and motion profile. At the system level, the model provides physical correlations between the DDM characteristic parameters, allowing for direct use of these parameters in HDPDMS optimization. By reducing the number of design parameters, models, and constraints in each level of optimization, the new framework can produce better results while reducing the optimization burden.

space through the optimization of DDM. Specifically, the search space is reduced from nine design parameters to five characteristic parameters in our case.

Traditional dimension reduction strategies based on design parameters depend on the motor topology. When the motor topology changes, a new dimension reduction strategy must be developed to select different design parameters. In contrast, our new dimension reduction strategy is tailored to a specific application, such as HDPDMS. As long as the application remains unchanged, the selection of the important characteristic parameters remains consistent, regardless of the motor topology. A similar optimization process can be performed for different motor topologies to optimize the HDPDMS, even if the design parameters vary. Thus, this method can be extended to other common motor topologies, such as using different rotor topologies (e.g., Halbach array and spoke array) or using various stator topologies, including different slot shapes and tooth tips.

When viewed from the perspective of the design parameter space, the traditional surrogate model allocates computational resources uniformly across the entire design parameter space. As a result, a considerable amount of computation resources are used on many redundant and unnecessary designs. Traditional dimensional reduction strategies involve replacing the complete design parameter space with a smaller

subspace of design parameters that contain the most relevant information. However, the computational resources are still allocated uniformly across the entire subspace. The new optimization framework employs optimization techniques to concentrate computational resources on the most relevant and useful regions of the design parameter space for better characteristic parameters, thereby minimizing wastage and conserving computation resources.

Based on the above analysis, the Performance comparison of the proposed approach and traditional optimization framework and surrogate model is shown in the Table 5.

VI. PROTOTYPE AND EXPERIMENT

We designed three DDMs corresponding to three different motion tasks, with motion tasks 1 and 3 using driver C and motion task 2 using driver B. We selected the designs that met the reliability indicators of -20% as shown in Figs 20, 22, and 21. Light loads and quick motion for motion task 2 called for a long and slender motor, while heavy loads and slow motion for motion task 3 required a short and pancake motor. The 3D view of these three frameless motors is depicted in Fig. 29.

To verify the effectiveness of our new optimization framework and the precision of the models used in the optimization process, we constructed a prototype for motion

TABLE 5. Performance comparison of the proposed approach, the traditional optimization framework, and the traditional surrogate model.

| Method		Proposed approach	Traditional framework	Traditional surrogate model
Component Surrogate model	Training dataset acquisition time	21 000 computation cases need 72 hours	No requirement for a surrogate model	10 077 696 computation cases need 1440 days
	Model training time	Training dataset includes 1820 uniform sampling needs 3 s		The time required for the creation of surrogate models is impractical
System optimization	Optimization time for one driver	0.25 hours	7 200 computation cases need 24 hours	
	Design parameters recovery time	0.25 hours	No need for design parameters recovery	
	Total time for motion task 1	Optimizations with three drivers and once design parameters recovery require 1 hour	Optimizations with three drivers require 72 hours	
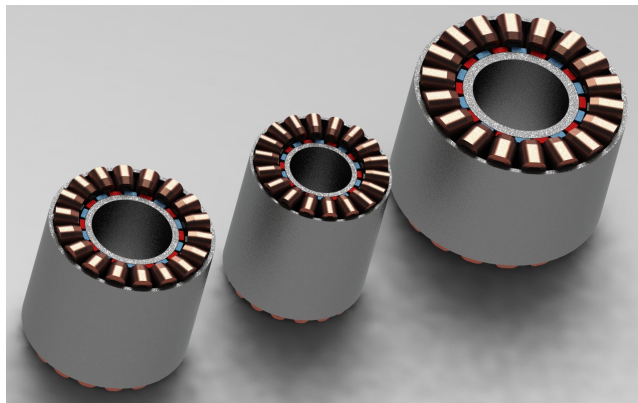
FIGURE 29. From left to right, the frameless motors correspond to three different motion tasks and vary in size, particularly for the motors in motion tasks 2 and 3. The need for light loads and quick motion results in a long and slender motor for motion task 2, while the need for heavy loads and slow motion leads to a short and stout motor for motion task 3. All the motors were generated using the same DDM optimization dataset and surrogate model through the optimization process described in section IV.

TABLE 6. Optimal design parameters of the HDPDMS for motion task 1.

Variable	Unit	Value
Current density (J_c)	A/mm^2	7.9
Thickness of the PMs ($r_3 - r_2$)	mm	4.0
PM opening angle ratio ($\alpha = \frac{\alpha'}{\alpha''}$)		0.89
Tooth length ($r_5 - r_4$)	mm	22.6
Stator yoke thickness, ($r_6 - r_5$)	mm	3.6
Width of tooth ratio ($\gamma = \frac{\gamma'}{\gamma''}$)		0.42
Active length (l)	mm	105.0
Outer radius (r_6)	mm	63.5
Inner radius (r_1)	mm	31.0
The total turns of the winding N_w		972
Jerk time ratio (Fig. 5) (α_s)		0.03
Constant time ratio (Fig. 5) (β_s)		0.273
Driver type		Driver C

TABLE 7. Motion profile parameters for motion task 1.

Variable	Unit	Value
Maximum velocity	rad/s	24.7
Maximum acceleration	rad/s^2	3692
Maximum jerk	rad/s^3	$6.14 \cdot 10^6$

task 1. The prototype, load, and experiment platform can be viewed in Fig. 30. To complete the motion task, we used driver C to drive the DDM with the load. We also tested the temperature of the winding using a PT-100 fixed to the winding of the DDM, and the temperature of the housing using a thermocouple. The optimal design parameters of the prototype are presented in Table 6. Additionally, we established the motion profile parameters for completing motion task 1, as listed in Table 7. Figure 31 illustrates the motion process, where each position involves a rotation angle of 18° and a motion time of 20 ms. Following the motion, a dwell time of 40 ms is allocated for chip sorting or inspection.

Figure 32 displays the current loop regulation with an update frequency of 20 kHz. We adjusted the bandwidth of the current loop to approximately 680 Hz with a 63° phase margin. Figure 33 shows the position and velocity loop regulation with an update frequency of 2 kHz. We adjusted the bandwidth of the position loop to approximately 80 Hz with a 40° phase margin.

Figure 34 presents the velocity and current curves during the motion time. From the figure, we can observe that the current tracks the current command, while the velocity feedback experiences a delay of 0.5 ms due to the 2 kHz update frequency of the velocity loop. The maximum current observed is approximately 25.2 A, which still has a 16% peak current margin with respect to the driver's 30 A peak current capacity. Similarly, the continuous current observed is approximately 11.6 A, which still has a 22% continuous current margin with respect to the driver's 15 A continuous current capacity.
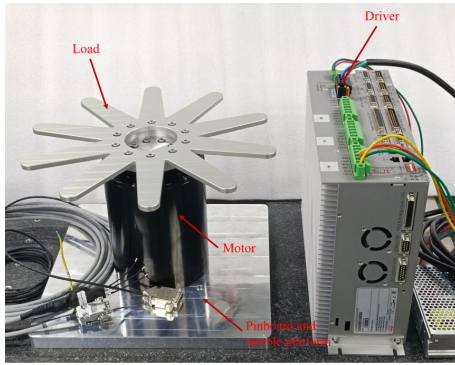
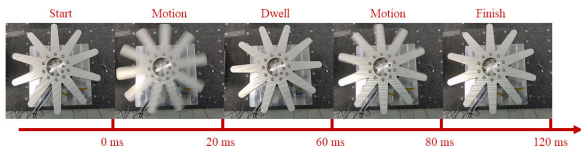**FIGURE 30.** Prototype and experiment platform.

FIGURE 31. Motion process. Each position involves a rotation angle of 18° and a motion time of 20 ms, followed by a 40 ms dwell time allocated for chip sorting or testing.
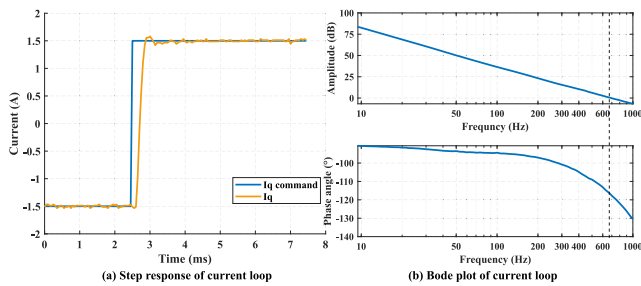

(a) Step response of current loop   (b) Bode plot of current loop

FIGURE 32. The current loop's step response and corresponding open-loop Bode plot.
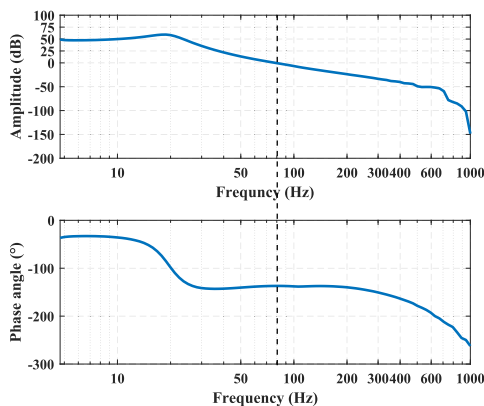
FIGURE 33. Open loop Bode plot of the position loop.

FIGURE 34. Velocity and current curve during the motion time. The current and velocity can track the current command and reference velocity, while the velocity feedback experiences a delay of 0.5 ms due to the 2 kHz update frequency of the velocity loop. The whole motion time is 20 ms which satisfies the motion task 1 requirement.

FIGURE 35. Temperatures rising of winding and housing. The test ambient temperature was about 20℃, and the temperature rise of the winding was about 51℃, which was smaller than our prediction (55℃) due to the heat dissipation from the mechanical load part, which is not taken into account in our thermal model.
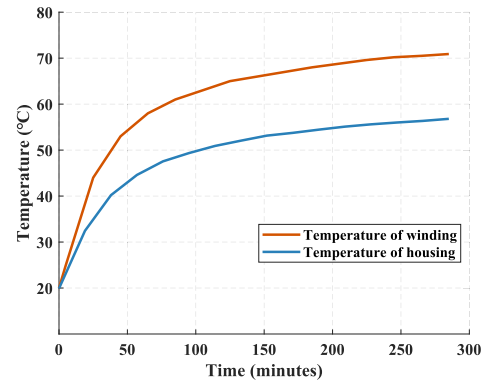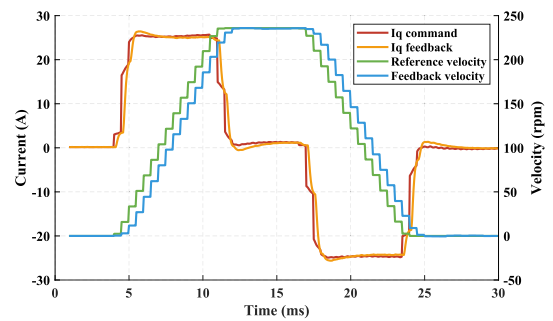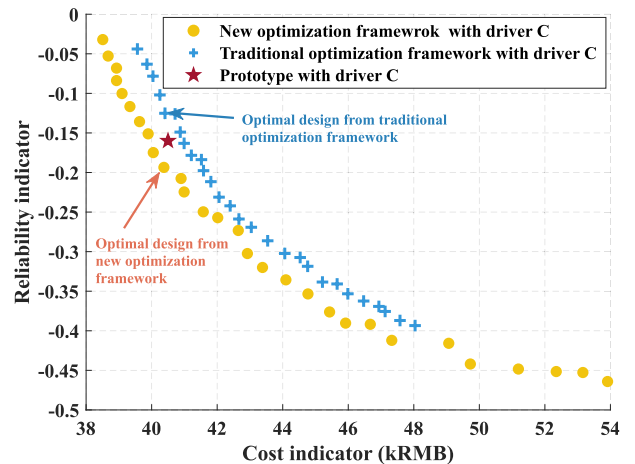

FIGURE 36. Prototype test result and Pareto front of new and traditional optimization framework.

Figure 35 displays the results of the thermal test. During the test, the ambient temperature was 20℃, and the winding temperature rose approximately 51℃. We assumed that the temperature rise of the winding would be the same at an ambient temperature of 25℃. The temperature of the winding would be 76℃, which is within the 24% margin of the upper limit of 100℃. This temperature was lower than our predicted

value of 80℃ due to our thermal model not accounting for heat dissipation from the mechanical load part in Fig. 30, which increased the heat dissipation surface and lowered the winding temperature. This error was acceptable due to the simplification of the thermal model. The prototype was able to perform well for motion task 1, as shown by the prototype test results on the Pareto front in Fig. 36. Due to

manufacturing and measurement limitations, the prototype's loss is greater than that of the theoretical model, resulting in slightly higher cost indicators. The prototype's reliability indicator was 16% due to the higher peak current, which is lower than the optimal design reliability indicator of 20% from the new optimization framework but still higher than the reliability indicator of 12% obtained from the traditional optimization framework. These results validate the effectiveness of the new optimization framework.

VII. CONCLUSION

This article presents a novel optimization framework for HDPDMS using surrogate models of characteristic parameters, which allows for quick and precise optimization of the entire system with limited computation resources. Unlike traditional optimization frameworks that combine all design parameters, models, and constraints, this new framework enables a separate optimization process at both the component level and system level through the use of surrogate models of characteristic parameters. During each optimization level, the component-level and system-level optimizations employ fewer design parameters, models, and constraints, effectively reducing the optimization burden and yielding better optimization results. Once the surrogate models are built, the framework could find the desired HDPDMS design for a specific motion task in just 1 hour, saving about 98.6% computation time compared to traditional methods. This tool is particularly useful for the initial design phase, which requires numerous adjustments to the motion control system.

Moreover, the new surrogate model uses optimization to centralize computation resources on the most useful search space, resulting in a 99.8% reduction in computation resources required to build the training dataset, compared to the traditional surrogate model, whose inputs are design parameters with full factorial sampling in our case. This new approach can be seen as a dimension reduction strategy that transfers the search space from the design parameters to the characteristic parameters of the components, as opposed to traditional dimension reduction strategies that only reduce the number of design parameters.

The new optimization framework provided is versatile. Firstly, it is not limited to any particular motor topology, making it unnecessary to conduct a sensitivity analysis and manually select important design parameters of the motor as required by traditional surrogate models. This means the method can be easily applied to different motor topologies for the HDPDMS. Secondly, the framework can absorb various optimization strategies to further reduce computation resources in both component-level and system-level optimizations. For instance, a pre-optimization using a quick analytical model can be applied during component-level optimization. Surrogate models can be substituted with alternative regression methods if those methods can offer sufficient prediction accuracy and can determine the boundaries of the input space. Similarly, the recovery method

for design parameters, such as the inverse surrogate model [32], [33], can also be replaced. This method establishes a mapping between the characteristic parameters and the design parameters. In future research, we will investigate the impact of various methods within this innovative optimization framework.

REFERENCES

[1] *Turret Test and Scan Handlers | Cohu*. Accessed: Apr. 9, 2023. [Online]. Available: https://www.cohu.com/handlers-turret-test-and-scan

[2] G. Lei, T. Wang, Y. Guo, J. Zhu, and S. Wang, "System-level design optimization methods for electrical drive systems: Deterministic approach," *IEEE Trans. Ind. Electron.*, vol. 61, no. 12, pp. 6591–6602, Dec. 2014.

[3] X. Sun, Z. Shi, G. Lei, Y. Guo, and J. Zhu, "Multi-objective design optimization of an IPMSM based on multilevel strategy," *IEEE Trans. Ind. Electron.*, vol. 68, no. 1, pp. 139–148, Jan. 2021.

[4] Y. Meng, S. Fang, Z. Pan, W. Liu, and L. Qin, "Machine learning technique based multi-level optimization design of a dual-stator flux modulated machine with dual-PM excitation," *IEEE Trans. Transport. Electrific.*, early access, 2022, doi: 10.1109/TTE.2022.3213083.

[5] X. Sun, N. Xu, and M. Yao, "Sequential subspace optimization design of a dual three-phase permanent magnet synchronous hub motor based on NSGA III," *IEEE Trans. Transport. Electrific.*, vol. 9, no. 1, pp. 622–630, Mar. 2023.

[6] P.-D. Pfister, X. Yin, and Y. Fang, "Slotted permanent-magnet machines: General analytical model of magnetic fields, torque, eddy currents, and permanent-magnet power losses including the diffusion effect," *IEEE Trans. Magn.*, vol. 52, no. 5, pp. 1–13, May 2016.

[7] M. Shen, P.-D. Pfister, C. Tang, and Y. Fang, "A hybrid model of permanent-magnet machines combining Fourier analytical model with finite element method, taking magnetic saturation into account," *IEEE Trans. Magn.*, vol. 57, no. 2, pp. 1–5, Feb. 2021.

[8] C. Tang, M. Shen, Y. Fang, and P.-D. Pfister, "Comparison of subdomain, complex permeance, and relative permeance models for a wide family of permanent-magnet machines," *IEEE Trans. Magn.*, vol. 57, no. 2, pp. 1–5, Feb. 2021.

[9] Y. Jin, H. Wang, T. Chugh, D. Guo, and K. Miettinen, "Data-driven evolutionary optimization: An overview and case studies," *IEEE Trans. Evol. Comput.*, vol. 23, no. 3, pp. 442–458, Jun. 2019.

[10] H. Zhao, C. Liu, Z. Song, and W. Wang, "Exact modeling and multiobjective optimization of Vernier machines," *IEEE Trans. Ind. Electron.*, vol. 68, no. 12, pp. 11740–11751, Dec. 2021.

[11] C. E. Rasmussen and C. K. I. Williams, *Gaussian Processes for Machine Learning*. Cambridge, MA, USA: MIT Press, Nov. 2005.

[12] A. Sobester, A. Forrester, and A. Keane, *Engineering Design Via Surrogate Modelling: A Practical Guide*. Hoboken, NJ, USA: Wiley, Sep. 2008.

[13] S. Giurgea, D. Fodorean, G. Cirrincione, A. Miraoui, and M. Cirrincione, "Multimodel optimization based on the response surface of the reduced FEM simulation model with application to a PMSM," *IEEE Trans. Magn.*, vol. 44, no. 9, pp. 2153–2157, Sep. 2008.

[14] Y. Duan and D. M. Ionel, "A review of recent developments in electrical machine design optimization methods with a permanent-magnet synchronous motor benchmark study," *IEEE Trans. Ind. Appl.*, vol. 49, no. 3, pp. 1268–1275, May 2013.

[15] Z. Pan and S. Fang, "Combined random forest and NSGA-II for optimal design of permanent magnet arc motor," *IEEE J. Emerg. Sel. Topics Power Electron.*, vol. 10, no. 2, pp. 1800–1812, Apr. 2022.

[16] Z. Pan, S. Fang, H. Wang, and Y. Zhong, "Accurate and efficient surrogate model-assisted optimal design of flux reversal permanent magnet arc motor," *IEEE Trans. Ind. Electron.*, vol. 70, no. 9, pp. 9312–9325, Sep. 2023.

[17] Z. Pan and S. Fang, "Torque performance improvement of permanent magnet arc motor based on two-step strategy," *IEEE Trans. Ind. Informat.*, vol. 17, no. 11, pp. 7523–7534, Nov. 2021.

[18] B. Hannon, P. Sergeant, L. Dupré, and P.-D. Pfister, "Two-dimensional Fourier-based modeling of electric machines—An overview," *IEEE Trans. Magn.*, vol. 55, no. 10, pp. 1–17, Oct. 2019.

[19] W. Lu, J. Zhu, Y. Fang, and P.-D. Pfister, "A hybrid analytical model for the electromagnetic analysis of surface-mounted permanent-magnet machines considering stator saturation," *Energies*, vol. 16, no. 3, p. 1300, Jan. 2023.

[20] J. Song, F. Dong, J. Zhao, H. Wang, Z. He, and L. Wang, "An efficient multiobjective design optimization method for a PMSLM based on an extreme learning machine," *IEEE Trans. Ind. Electron.*, vol. 66, no. 2, pp. 1001–1011, Feb. 2019.

[21] G. Lei, C. Liu, J. Zhu, and Y. Guo, "Techniques for multilevel design optimization of permanent magnet motors," *IEEE Trans. Energy Convers.*, vol. 30, no. 4, pp. 1574–1584, Dec. 2015.

[22] G. Lei, K. R. Shao, Y. Guo, J. Zhu, and J. D. Lavers, "Sequential optimization method for the design of electromagnetic device," *IEEE Trans. Magn.*, vol. 44, no. 11, pp. 3217–3220, Nov. 2008.

[23] G. Lei, X. M. Chen, J. G. Zhu, Y. G. Guo, W. Xu, and K. R. Shao, "Multiobjective sequential optimization method for the design of industrial electromagnetic devices," *IEEE Trans. Magn.*, vol. 48, no. 11, pp. 4538–4541, Nov. 2012.

[24] G. Ellis, *Control System Design Guide: Using Your Computer to Understand and Diagnose Feedback Controllers*. London, U.K.: Butterworth, Jun. 2012.

[25] D. H. Gurocak, *Industrial Motion Control: Motor Selection, Drives, Controller Tuning, Applications*. Hoboken, NJ, USA: Wiley, Mar. 2016.

[26] P.-D. Pfister, C. Tang, and Y. Fang, "A multi-objective finite-element method optimization that reduces computation resources through subdomain model assistance, for surface-mounted permanent-magnet machines used in motion systems," *IEEE Access*, vol. 11, pp. 8609–8621, 2023.

[27] Q. Chen, Z. Zou, and B. Cao, "Lumped-parameter thermal network model and experimental research of interior pmsm for electric vehicle," *CES Trans. Electr. Mach. Syst.*, vol. 1, no. 4, pp. 367–374, Dec. 2017.

[28] J.-Y. Ryu, S.-W. Hwang, J.-W. Chin, Y.-S. Hwang, S. W. Yoon, and M.-S. Lim, "Mathematical modeling of fast and accurate coupled electromagnetic-thermal analysis," *IEEE Trans. Ind. Appl.*, vol. 57, no. 5, pp. 4636–4645, Sep. 2021.

[29] M. Li, S. Yang, and X. Liu, "Pareto or non-Pareto: Bi-criterion evolution in multiobjective optimization," *IEEE Trans. Evol. Comput.*, vol. 20, no. 5, pp. 645–665, Oct. 2016.

[30] K. Deb, A. Pratap, S. Agarwal, and T. Meyarivan, "A fast and elitist multiobjective genetic algorithm: NSGA-II," *IEEE Trans. Evol. Comput.*, vol. 6, no. 2, pp. 182–197, Apr. 2002.

[31] J. H. Holland, *Adaptation in Natural and Artificial Systems: An Introductory Analysis With Applications to Biology, Control, and Artificial Intelligence*. Cambridge, MA, USA: MIT Press, Apr. 1992.

[32] S. Koziel, M. A. Belen, A. Çalişkan, and P. Mahouti, "Rapid design of 3D reflectarray antennas by inverse surrogate modeling and regularization," *IEEE Access*, vol. 11, pp. 24175–24184, 2023.

[33] I. Couckuyt, D. Gorissen, T. Dhaene, and F. De Turck, "Inverse surrogate modeling: Output performance space sampling," in *Proc. 13th AIAA/ISSMO Multidisciplinary Anal. Optim. Conf.*, Sep. 2010, p. 9393.

CHENTAO TANG was born in Jiangsu, China, in 1995. He received the B.S. degree in electrical engineering from the Nanjing Institute of Technology, Nanjing, China, in 2018. He is currently pursuing the Ph.D. degree with Zhejiang University, Hangzhou, China.

His research interests are in the field of permanent-magnet machines and motion control systems.

XIN YIN (Member, IEEE) was born in Gaoyou, Jiangsu, China. He received the Ph.D. degree in electrical engineering from Zhejiang University, Hangzhou, China, in 2017.

He is currently the Research and Development Director with Akribis Systems. His research interests include design and application of direct drive motors and systems.

YOUTONG FANG (Senior Member, IEEE) received the B.S. and Ph.D. degrees in electrical engineering from the Hebei University of Technology, Hebei, China, in 1984 and 2001, respectively.

Currently, he is a Professor with the College of Electrical Engineering, Zhejiang University, Hangzhou, China. His research interests include the application, control, and the design of electrical machines.

Dr. Fang achieved the second prize of the National Scientific and Technological Progress Award twice, the first prize of Provincial Science and Technology Progress Award twice and the first prize of Provincial Science and Technology Progress Award three times.

PIERRE-DANIEL PFISTER (Member, IEEE) was born in Bienne, Switzerland, in 1980. He received the M.Sc. and Ph.D. degrees in physics from the Swiss Federal Institute of Technology, Lausanne (EPFL), Switzerland, in 2005 and 2010, respectively.

He is currently an Associate Professor with Zhejiang University, Hangzhou, China. His current research interests include permanent-magnet machines, very-high-torque-density machines, analytical optimization, and robotics.

• • •